PCCP

Check for updates

Effect of electric fields on tungsten distribution in Na$_2$WO$_4$–WO$_3$ molten salt

Yuliang Guo,[a] Xiaobo Sun,[ab] Handong Jiao, [iD][c] Liwen Zhang,[ab] Wenxuan Qin,[d] Xiaoli Xi [iD]*[ae] and Zuoren Nie*[abe]

Tungsten coatings have unique properties such as high melting points and hardness and are widely used in the nuclear fusion and aviation fields. In experiments, compared to pure Na$_2$WO$_4$ molten salt, electrolysis with Na$_2$WO$_4$–WO$_3$ molten salt results in a lower deposition voltage. Herein, an investigation combining experimental and computational approaches was conducted, involving molecular dynamics simulations with deep learning, high-temperature *in situ* Raman spectroscopy and activation strain model analysis. The results indicated that the molten salt system's behaviour, influenced by migration and polarization effects, led to increased formation of Na$_2$W$_2$O$_7$ in the Na$_2$WO$_4$–WO$_3$ molten salt, which has a lower decomposition voltage and subsequently accelerated the cathodic deposition of tungsten. We analyzed the mechanism of the effect of the electric field on the Na$_2$W$_2$O$_7$ structure based on the bond strength and electron density. This research provides crucial theoretical support for the effect of electric field on tungsten in molten salt and demonstrates the feasibility of using machine learning-based DPMD methods in simulating tungsten-containing molten salt systems.

Introduction

Tungsten is a rare refractory metal with exceptional physico-chemical properties, including high melting point and great hardness, making it promising for applications in many fields like fusion devices and aerospace.[1–3] The Na$_2$WO$_4$–WO$_3$ molten salt system is predominantly utilized for tungsten coating since WO$_3$ is stable and relatively easy to prepare.[4–6] Electrodeposition of tungsten with molten salts as a medium is an effective approach in the production of tungsten coatings[7–12] and has garnered considerable attention.[13–18] In terms of electrode selection, studies have suggested that copper electrodes in Na$_2$WO$_4$–WO$_3$ molten salt can produce dense tungsten coatings.[19,20] Nevertheless, few theoretical research studies were conducted to reveal the mechanism in the process of tungsten coating.[21–23] First-principles molecular dynamics simulation is useful for a deep understanding of the

mechanisms, although accurate to study statistical properties of the molten salt system, such as radial distribution functions (RDF); however, it requires substantial computational resources. Electric fields may have an impact on reactions in solutions,[24] and the research on this effect in molten salts is of great significance for understanding the principles of electrodeposition.

The development of machine learning methods brings more possibilities in mechanism research.[25,26] There have been reports on the application of deep potential molecular dynamics (DPMD),[27] a machine learning based molecular dynamics simulation method with first-principles accuracy. DPMD has been used to study molten salts with thermo-dynamics.[28–30] The deposition potential of the system is obtained by calculating the Gibbs free energy of the system,[31] and the effect of temperature on the molten salt system is studied by calculating parameters such as RDF and viscosity.[32] As far as we know, there are no research studies on molten salt systems containing tungsten using machine learning methods like DPMD. The expansion of DPMD under similar systems is also of great importance. This work also conducts simulation and experimental analysis on systems different from the training data set. This innovative application demonstrates good accuracy while saving significant computing resources.

In this work, we studied the composition and electro-chemical properties of Na$_2$WO$_4$ and Na$_2$WO$_4$–WO$_3$ molten salts through the electrolysis, which indicate that, compared to Na$_2$WO$_4$ molten salt, the existence of WO$_3$ species lead to a

[a] *Collaborative Innovation Center of Capital Resource-Recycling Material Technology, College of Materials Science and Engineering, Beijing University of Technology, Beijing 100124, China. E-mail: xixiaoli@bjut.edu.cn*

[b] *National Engineering Laboratory for Industrial Big-data Application Technology, Beijing University of Technology, Beijing 100124, China*

[c] *Institute of Advanced Structure Technology, Beijing Institute of Technology, Beijing 100081, China*

[d] *School of Chemistry and Materials Engineering, Xinxiang University, Xinxiang, Henan 453003, China*

[e] *Key Laboratory of Advanced Functional Materials, Ministry of Education, Beijing University of Technology, Beijing 100124, China*

lower deposition voltage. We then employed the DPMD method to acquire a potential energy function from a database generated by CP2K.[33] Subsequently, we applied this potential energy function in LAMMPS[34] to perform larger-scale molecular dynamics simulations with first-principles precision. The analysis of simulation results under various temperature and voltage conditions not only verifies the accuracy of the simulation outcomes but also provides further insights into why tungsten deposits more readily in Na_2WO_4–WO_3 molten salt and the specific mechanism with the bond strength and electron density. This work provides essential theoretical guides for the development of tungsten coating processes.

Method

This work includes the following three parts of experimental content. First, the deposition conditions of tungsten in different molten salt systems were analysed in electrochemical experiments. Next, molecular dynamics simulations with deep potential were performed to analyse the effects of temperature and electric field on tungsten deposition in the Na_2WO_4–WO_3 molten salt system. Finally, high-temperature *in situ* Raman tests were conducted on Na_2WO_4–WO_3 molten salt under different voltages to verify the results of molecular dynamics simulations.

Electrochemical experiments

In the electrodeposition experiments and electrochemical tests, the molten salts of Na_2WO_4 and Na_2WO_4–WO_3 (molar ratio: 3 : 1) were heated to 1173 K in a tube furnace with argon atmosphere and kept for 3 hours to melt fully. The electrodeposition process and electrochemical measurements are controlled by the electrochemical workstation VersaSTAT4 (AMETEK-Drexelbrook). A three-electrode system was used in the electrochemical test, in which a W rod was the auxiliary electrode, Pt wire was the reference electrode, and Pt wire or Cu wire was the working electrode. A two-electrode system was used in the electrodeposition experiment, with the anode being a W rod and the cathode being a Cu sheet, and the

electrodeposition experiment was conducted at 40 mA cm^{-2} for 5 h. Electrodeposition and electrochemical testing are performed by inserting electrodes into molten salt. XRD (XRD-7000) was used for composition analysis of Na_2WO_4 and Na_2WO_4–WO_3 molten salt supernatants.

High-temperature *in situ* Raman data

The high-temperature *in situ* Raman data were obtained by a multipurpose operando instrument for high-temperature electrochemistry,[35] as illustrated in Fig. 1a. This instrument integrates essential components, including Raman spectroscopy, optical microscopy, and a highly precise electrical heating stage. The detachable electrode equipment and the gas path design in the high-temperature pool make it possible to conduct *in situ* Raman tests in an argon atmosphere to observe the effect of the electric field on the microstructure of the molten salt at high temperatures. Anhydrous Na_2WO_4 and WO_3 with a molar ratio of 3 : 1 was heated to 1173 K with a constant speed in a tube furnace and kept for 3 hours to completely melt, then cooled for later use. The *in situ* Raman test was performed in an argon atmosphere at 973 K. Fig. 1b shows the high-temperature *in situ* Raman test process, under the voltage conditions of 0.4 V, 0.8 V, 1.2 V and 1.4 V. Each voltage is maintained for two minutes and then the Raman signal is collected for three minutes. After the acquisition is completed, the voltage returns to zero.

Molecular dynamic simulations with DPMD

In this experiment, as illustrated in Fig. 2, AIMD calculation was implemented using the DeepMD-kit software package (v2.1.1),[36,37] Initially, *ab initio* molecular dynamics simulations were conducted using CP2K (version 2023.1)[33,38] to generate the dataset to train the DPMD potential function. The interatomic potential was calculated at the density functional theory level, using the van der Waals modified PBE density functional with reference to the AIMD simulation of the halogen molten salt system. The MOLOPT basis with double-zeta valence polarized quality was selected for the elements (Na, W, and O), a plane
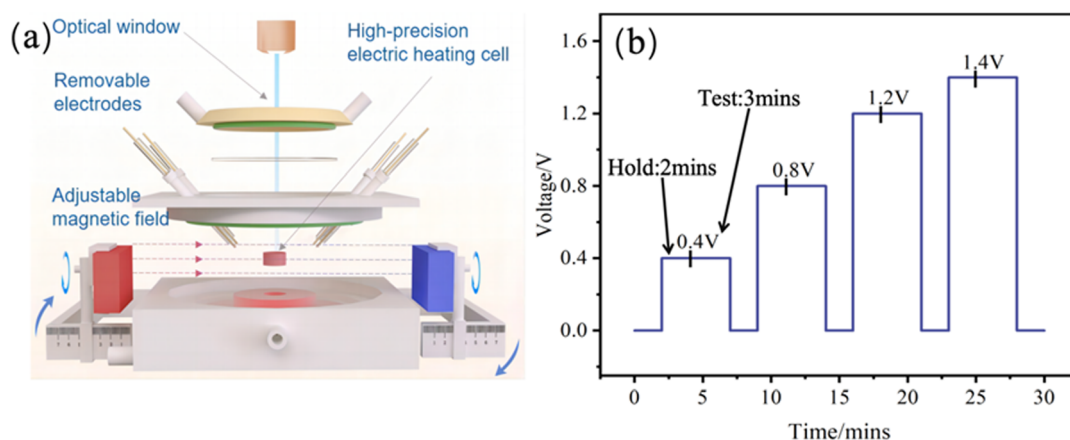

Fig. 1 (a) High-temperature *in situ* Raman instrumentation;[35] and (b) voltage conditions during Raman measurement.
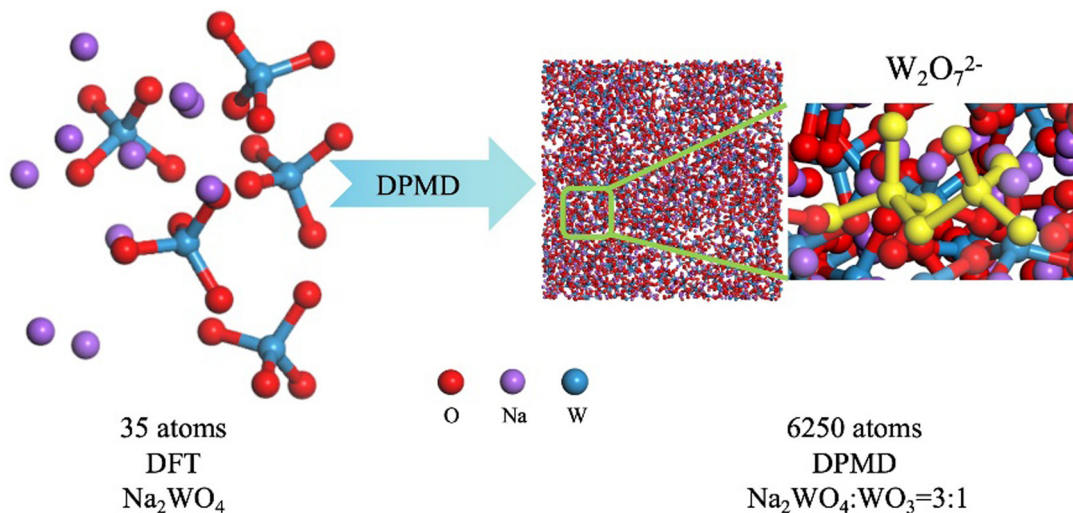
Fig. 2 Training DPMD in the AIMD dataset and enabling large-scale molecular dynamics with first-principles precision.

wave cutoff of 1400 Ry adopted for the expansion of the electron density in reciprocal space.

An initial simulation box of Na_2WO_4 was constructed, containing $10Na^+$ ions and $5WO_4^{2-}$ ions. The calculations were performed at temperatures of 1173 K, and molecular dynamics simulations utilized the NVT ensemble with the Nose–Hoover thermostat. A timestep of 1 fs was selected, the simulations were run for a total of 25 ps to gather an extensive dataset for training. Multiwfn software (version 3.8)[39] was used for preparing the input files for CP2K.

For molten salts composed of elements with smaller atomic numbers, such as NaCl and $MgCl_2$, the initial structure typically includes 50–150 atoms.[29,31,32] However, for systems with larger atomic numbers like tungsten, excessively large systems may require computationally prohibitive resources. Efficient computational methods are thus significant for these types of systems. Therefore, in this work, we constructed a system containing 35 atoms and validated our simulation results with experimental methods. This approach helps explore the minimum number of atoms required in the original system for accurate simulation results using deep potential training. A dataset of 25 000 frames has already been proven sufficient for the convergence of neural network training in related molten salt studies.[31,32]

The DeepMD-Kit software package, a program for neural network training and evaluation of atomic energies and forces with machine learning, is utilized to create deep potentials for molten Na_2WO_4. This software employs deep neural networks for modeling interatomic interaction potentials, enabling high precision and efficiency in molecular dynamics simulations. The software converts the structural information of atoms into numerical representations that can be processed by neural networks. DeepMD-kit consists of two parts, first obtaining the descriptor of the atomic environment, and then mapping the descriptor to a fitting network of energy and atomic forces. Regarding the descriptor part, the software uses an algorithm

called Deep Potential Smooth Edition (DeepPot – SE), which can automatically obtain all angle and radial information in the atomic system. The construction of descriptors is provided as follows: the cutoff radius (rcut) for this process was determined through a combination of training cost and computational accuracy considerations, ultimately settling on a value of 6.0. The selected number (sel) of atoms in rcut is {15, 35, 20}, automatically calculated by the DeepMD-kit, which represents the maximum number of W, O, and Na in rcut. In order to set up a residual network structure,[40] the embedding net includes three hidden layers [25, 50, 100], and the outer layer always has twice the number of layers. In addition, the learning rate of the system is based on the official recommended value, which is starting from 0.001 and decays to 3.51×10^{-8} every 5000 steps in an exp manner.

The trained model was employed for molecular dynamics simulations using LAMMPS software (version 23Jun2022). The Na_2WO_4–WO_3 box consisted of 250 WO_3 units, 750 WO_4^{2-} ions and 1500 Na^+ ions. Simulations were conducted under the NVT ensemble at temperatures of 1173 K, 1200 K, 1250 K, and 1300 K to investigate the influence of temperature on the system's structure. An electric voltage was applied in the x-direction to study the impact of an electric field on the system's microstructure.

Activation strain model analysis

In order to elaborate on the bonding mechanism of the formation of W–O bond (O_4W^{2-}–WO_3) and how this bond strength changes under different electric fields, the activation strain model analysis was performed using the Amsterdam Density Functional (ADF 2023)[41] using relativistic density functional theory at the ZORA-PBE/TZ2P level. All computations were carried out in the gas phase and through vibrational analysis, and all energy minima were confirmed to be zero imaginary frequencies. The activation strain model of chemical reactivity[42,43] is a fragment-based approach to understand the

6592 | *Phys. Chem. Chem. Phys.*, 2024, **26**, 6590–6599

This journal is © the Owner Societies 2024
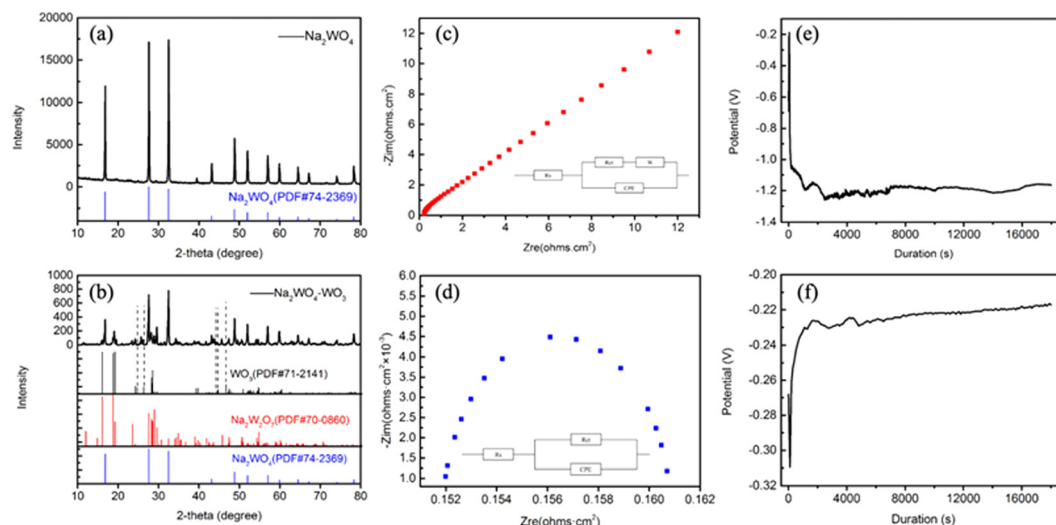
Fig. 3 Composition and electrochemical variations between Na_2WO_4 and Na_2WO_4–WO_3 molten salts. (a) XRD of the supernatant in Na_2WO_4 molten salt; (b) XRD of the supernatant in Na_2WO_4–WO_3 molten salt; (c) AC impedance spectrum and equivalent circuit diagram of Na_2WO_4 molten salt; (d) AC impedance spectrum and equivalent circuit diagram of Na_2WO_4–WO_3 molten salt; (e) electrolysis curve of Na_2WO_4 molten salt; and (f) electrolysis curve of Na_2WO_4–WO_3 molten salt.

energy profile of a chemical process and to explain it in terms of the original reactants. In this work, we only focus on the stationary point of the product. This allows an easy assessment of the influence of geometrical deformation and electronic structure of the catalyst and substrate. The bonding energy ΔE is decomposed into the strain energy ΔE_{strain} that is associated with the geometrical deformation of the individual reactants as the process takes place, plus the actual interaction energy ΔE_{int} between the deformed reactants. Furthermore, the strain energy ΔE_{strain} can be split into contributions from the deformation of the substrate and that of the catalyst (see eqn (1)).

$$\Delta E = \Delta E_{strain} + \Delta E_{int} \tag{1}$$

$$\Delta E_{int} = \Delta V_{elstat} + \Delta E_{Pauli} + \Delta E_{oi} \tag{2}$$

The interaction energy ΔE_{int} between the deformed reactants is further analyzed in the conceptual framework provided by the Kohn–Sham molecular orbital (KS-MO) model, using a quantitative energy decomposition scheme (see eqn (2)). The term Velstat corresponds to the classical Coulomb interaction between the unperturbed charge distributions of the deformed reactants and the Pauli repulsion energy ΔE_{Pauli} comprises the destabilizing interactions between occupied orbitals on the respective reactants and is responsible for steric repulsion. The orbital interaction energy ΔE_{oi} accounts for charge transfer and polarization.

Results and discussion

Electrolysis of Na_2WO_4–WO_3 molten salt

Fig. 3a and b show the XRD patterns of the quenched Na_2WO_4 and Na_2WO_4–WO_3 molten salt supernatant. The physical phase in the Na_2WO_4 molten salt system is still the unit Na_2WO_4,

which suggests the hexavalent tungsten ions are reduced at the cathode in the form of WO_4^{2-}. In the Na_2WO_4–WO_3 molten salt system, there are Na_2WO_4, $Na_2W_2O_7$ and WO_3, among which the characteristic peak intensity of WO_3 is smaller, indicating that the molten salt contains less WO_3. As above, the forms of hexavalent tungsten in the molten salt system include WO_3, WO_4^{2-} and $W_2O_7^{2-}$. We finally inferred that WO_3 reacts with Na_2WO_4 in the molten salt to generate $Na_2W_2O_7$. Therefore, the possible decomposition reactions that may occur in molten salt include $Na_2WO_4 = Na_2O + W + 3/2O_2(g)$, $Na_2W_2O_7 = W + Na_2WO_4 + 3/2O_2$ (g), and $WO_3 = W + 3/2O_2(g)$. Based on $\Delta G_T^{\theta} = -nFE_T^{\theta}$, we calculated the theoretical decomposition voltage for each reaction. At 1173 K, the theoretical decomposition voltages of Na_2WO_4, WO_3 and $Na_2W_2O_7$ which may be used as tungsten sources in Na_2WO_4–WO_3 molten salt system containing the $Na_2W_2O_7$ phase are 1.483 V, 0.9392 V and 0.9240 V, respectively. It can be found that the theoretical decomposition voltage of $Na_2W_2O_7$ is the lowest among the three tungsten compounds. Therefore, it is considered that the hexavalent tungsten ion in the form of $W_2O_7^{2-}$ will produce an electroreduction reaction on the surface of the copper cathode to realize the electrochemical deposition of tungsten coating on the cathode sheet.

In order to elucidate the reduction process of tungsten ions, as the Fig. 3c and d, electrochemical impedance spectroscopy tests were conducted on the Na_2WO_4 and Na_2WO_4–WO_3 molten salt systems under the conditions of an applied potential of -0.6 V on the Cu electrode. The electrochemical impedance spectrum of pure Na_2WO_4 molten salt presents a semicircle at high frequencies and a straight line at low frequencies, indicating that the electrodeposition process of tungsten ions on the cathode is controlled by a mixture of charge transfer and ion diffusion. The electrochemical impedance spectrum of Na_2WO_4–WO_3 molten salt only shows semicircular

This journal is © the Owner Societies 2024

Phys. Chem. Chem. Phys., 2024, **26**, 6590–6599 | **6593**

features at high frequencies. At this time, the electrochemical deposition process in the molten salt system is mainly controlled by charge transfer. Among the components of the equivalent circuit, R_s is the resistance generated by the ion conductor (molten salt) and the electronic conductor (electrode material), which is the liquid phase resistance; CPE is the constant phase angle component, which can be used to describe the interface electric double layer capacitance of the Cu electrode and molten salt; R_{ct} is the charge transfer resistance of the reaction process; W is the Warburg impedance element. From the impedance value obtained by fitting in Fig. 3c, the liquid phase resistance R_s on the cathode in Na_2WO_4 molten salt is 0.205 Ω cm^2, and the charge transfer resistance R_{ct} is 0.790 Ω cm^2. For the Na_2WO_4–WO_3 molten salt system, the impedance value obtained in Fig. 3d shows that the liquid phase resistance R_s on the Cu cathode is 0.152 Ω cm^2, and the charge transfer resistance R_{ct} is 0.009 Ω cm^2. Compared with the impedance in Na_2WO_4 molten salt, the charge transfer resistance decreased by 2 orders of magnitude, indicating that the reduction of tungsten ions is easier in the Na_2WO_4–WO_3 molten salt system.

In the electrodeposition experiment, the electrolytic cell voltage in the Na_2WO_4 molten salt rises rapidly in the early stage of electrolysis, gradually stabilizes, and finally stays between 1.1–1.2 V, as the Fig. 3e. In Fig. 3f, the electrolytic cell voltage in the Na_2WO_4–WO_3 molten salt system finally stabilizes at around −0.22 V after a long period of electrolysis. Compared with the electrolytic cell voltage in the Na_2WO_4 system, the cell voltage in the Na_2WO_4–WO_3 system dropped by about 1 V.

DPMD simulation and verification

We employed deep potential molecular dynamics (DPMD) for training on the Na_2WO_4 system at 1173 K, without the influence of an electric field, as depicted in Fig. 4. Fig. 4a and b illustrate the root mean square error (RMSE) of energy and forces during the DPMD training process for this system. A descending trend observed in the scatter plot indicates that the system began converging from 400 000 steps onward. The top-right portion of the figure elucidates the RMSE over the final 5000 steps of the training process, where the RMSE for energy is less than 0.2%, and slightly above 0.8% for forces. The training phase reached completion, establishing a mostly continuous and stable molten salt system. To evaluate the accuracy of the model, 100 sets of energy and forces data were predicted using this model, as shown in Fig. 4c and d. The agreement between density functional theory (DFT) and DPMD demonstrates the accuracy of DPMD in simulating the molten salt behaviour of this system.

Effect of temperature on the microstructure of the molten salt

The model trained by DPMD conduct molecular dynamics simulations of the Na_2WO_4–WO_3 molten salt system at different temperature with no electric field, and the coordination number and RDF of the W–O bond was analysed, as depicted in Fig. 5.

Fig. 5a and b shows the RDF and coordination number of W–O bonds at different temperatures without adding an electric field. Because the molecular dynamics simulation sets periodic boundary conditions, the coordination number hardly changes as the temperature rises. The peak of RDF appears at 1.782 Å, and then gradually decreases as temperature rises, which indicates that the rise of temperature increases the chaos of the system. The work of Tingrui Xu proved the accuracy of this conclusion. They performed DPMD simulations on $MgCl_2$–NaCl and $MgCl_2$–KCl molten salts. As the temperature increased, the peak value of the RDF also declined as
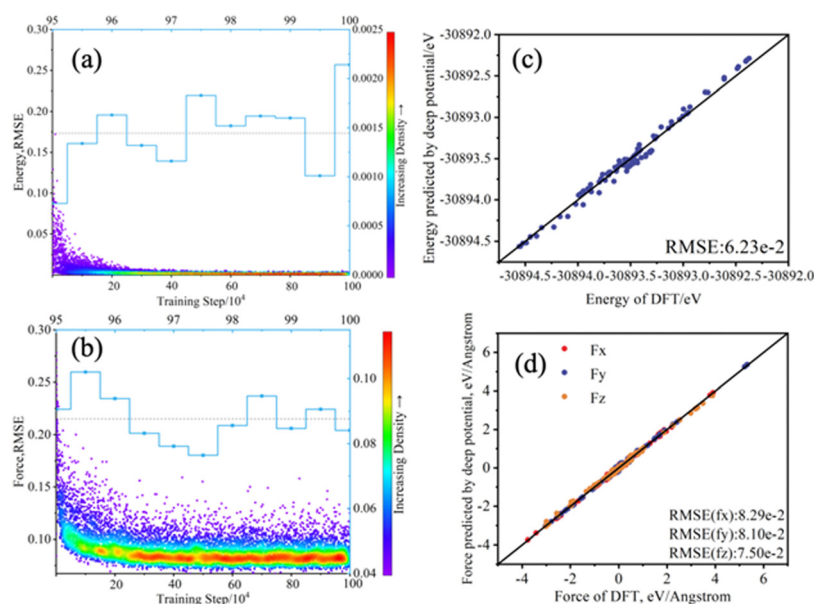

Fig. 4 (a) Root mean square error (RMSE) of energy during DPMD training process; (b) root mean square error (RMSE) of forces during DPMD training process; (c) forces of the system as predicted by DPMD and calculated by DFT; (d) energy of the system as predicted by DPMD and calculated by DFT.
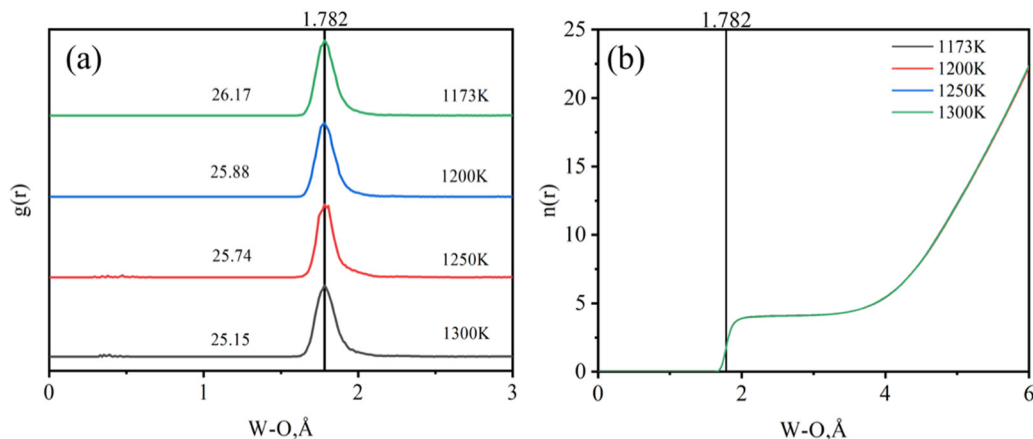
6594 | *Phys. Chem. Chem. Phys.*, 2024, **26**, 6590–6599

This journal is © the Owner Societies 2024

Fig. 5 (a) RDF of W−O of Na_2WO_4–WO_3 molten salt at different temperatures; (b) coordination number of W−O of Na_2WO_4–WO_3 molten salt at different temperatures.

mentioned above. Besides, there was no correlation between temperature and tungsten distribution in molten salt systems.

Effect of electric field on the microstructure of the molten salt

Furthermore, molecular dynamic simulation with deep potential was conducted for the Na_2WO_4–WO_3 molten salt system at 1173 K under voltage conditions of 0 V, 0.4 V, 0.8 V and 1.2 V. As shown in Fig. 6, we analyzed the RDF and coordination number of W–O in the simulation results. Migration in the electric field cannot be simulated under periodic boundary conditions, RDF indicates the structural rearrangement of the ionic groups with the polarization caused by the electric field, which makes the system more inclined to bond at 1.782 Å. Materials studio 2020 was performed for the structural optimization of WO^{4-}, WO_2^{2-}, WO_3^{-}, WO_4^{2-}, and $W_2O_7^{2-}$. The results of structural optimization are shown in Table 2, and only the bond with a length of 1.782 Å exists in the $W_2O_7^{2-}$ structure. The polarization effect with the electric field in Na_2WO_4–WO_3 molten salt will increase the tendency of the system to generate $W_2O_7^{2-}$.

In particular, molecular dynamics simulation with DPMD was performed on the system under voltage conditions of 0–1.2 V, and the results are shown in Fig. 7. Fig. 7a shows the RDF with a W–O bond length of 1.782 Å in the DPMD simulation results under different voltage conditions. As the voltage increases, the RDF of 1.782 Å gradually increases, which indicates that the increase in voltage increases the distribution probability of W–O bonds here. The number of W–O bonds with a length of 1.782 Å (± 0.005) in the system was calculated, as shown in Fig. 7b. The red part in the figure is the WO bond with a length of 1.782 Å, and the blue part is other WO bonds less than 1.95 Å. Corresponding to Fig. 7a, as the voltage increases, the total number of W–O bonds in the system does not change significantly, but the number of W–O bonds with a length of 1.782 Å gradually increases. Combined with the information in Table 1, the more $Na_2W_2O_7$ is generated in the system under the electric field.

In order to verify this simulation, we conducted high-temperature *in situ* Raman tests on the Na_2WO_4–WO_3 molten salt system. Fig. 8a shows the test results of high-temperature *in situ* Raman, and Fig. 8b is a partial enlargement of the wavelength range of 900–1000 cm^{-1}.

Referring to the Raman tests of related systems in the literature,[44,45] the structure vibrating in the wavelength range
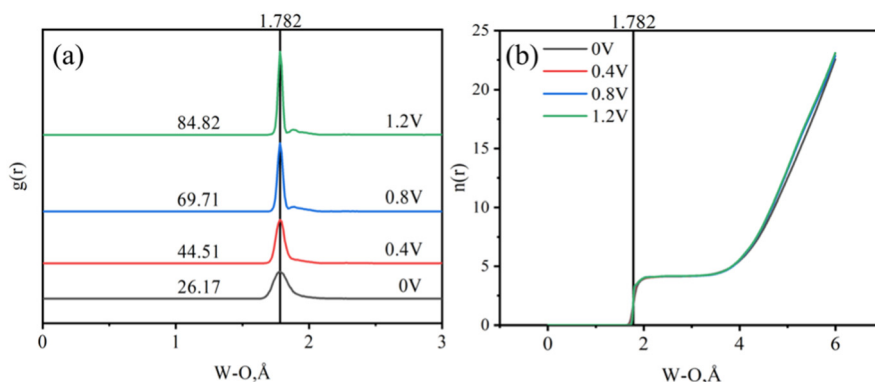

Fig. 6 (a) RDF of W−O of Na_2WO_4–WO_3 molten salt at different voltages; (b) coordination number of W−O of Na_2WO_4–WO_3 molten salt at different voltages.

This journal is © the Owner Societies 2024

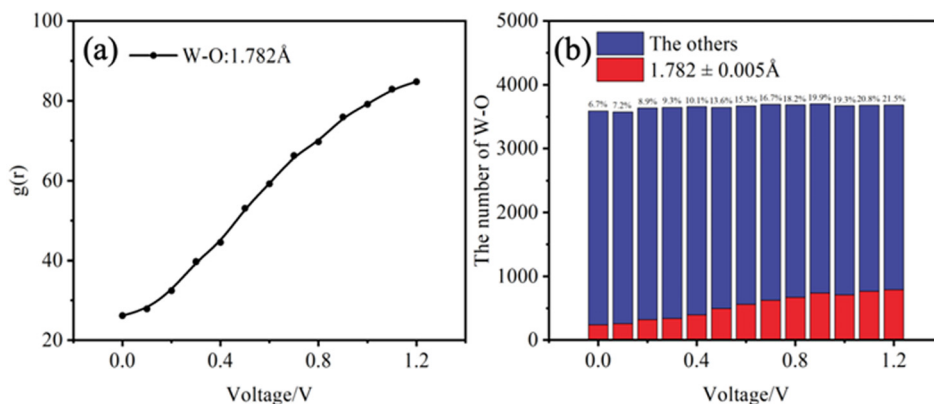*Phys. Chem. Chem. Phys.*, 2024, **26**, 6590–6599 | **6595**

Fig. 7 (a) RDF peak value at different voltages; (b) the number of W−O bonds at 0−1.2 V.

Table 1 Bond length and angle information of each structure in the system

	Length/Å	Angle/°
WO^{4-}	1.678	—
WO_2^{2-}	1.810	113.351
WO_3^-	1.820	102.994
WO_4^{2-}	1.811	109.471
$W_2O_7^{2-}$	1.782/1.930	108.456/110.662

of 321–486 cm^{-1} is mainly caused by the W–O bond vibration in Na$_2$WO$_4$, and 832–932 cm^{-1} corresponds to the W–O bond in Na$_2$W$_2$O$_7$. As the voltage increases, the Raman signal intensity of the W$_2$O$_7^{2-}$ structure decreases significantly. Considering the migration of ionic groups with the electric field, it suggests the main transferred group in this molten salt system is W$_2$O$_7^{2-}$. Compared with WO$_4^{2-}$, the W$_2$O$_7^{2-}$ anion is prone to react at the anode, whereas the tungsten element tends to deposit at the cathode. Specifically, from a microscopic perspective, the W$_2$O$_7^{2-}$ makes the oxygen ions reach the anode and react with a lower voltage. In Fig. 8b, the concentration of the W$_2$O$_7^{2-}$ structure shows a trend of first decreasing and then increasing as the voltage increases from 0 V to 0.8 V, which is caused by the polarization of the ionic groups in the molten salt

Table 2 Activation strain analysis of O$_4$W^{2-}−WO$_3$ bond in W$_2$O$_7^{2-}$ without the electric field ($F = 0$) and under the electric fields ($F = 0.1, 0.4, 1.0$ V Å^{-1})^a

ASM (in kcal mol^{-1})	0	0.1	0.4	1.0
$\Delta E_{strain}[\text{"}WO_4^{2-}\text{"}]$	5.7	−2.6	−27.5	−77.4
$\Delta E_{strain}[\text{"}WO_3\text{"}]$	2.7	2.6	2.3	1.9
ΔE_{strain}	8.4	0	−25.2	−75.5
ΔV_{elstat}	−203.6	−204.4	−210.9	−246.0
ΔE_{Pauli}	163.6	161.8	157.4	151.7
ΔE_{oi}	−122.5	−120.0	−113.2	−102.5
ΔE_{int}	−162.5	−162.6	−166.7	−189.8
ΔE	−154.1	−162.6	−191.9	−265.3

^{a} Computed at ZORA-PBE/TZ2P.

with the electric field. This electric field is more inclined to generate the W$_2$O$_7^{2-}$ structure, which confirms the previous DPMD simulation results.

In order to understand how and why the bond strength changes in the presence of different electric fields, we perform the activation strain model analysis on the O$_4$W^{2-}–WO$_3$ bond in W$_2$O$_7^{2-}$ without the electric field ($F = 0$) and under electric fields ($F = 0.1, 0.4, 1.0$ V Å^{-1}). All data are collected in Table 2 and to make the trends clearer, the related plots of different
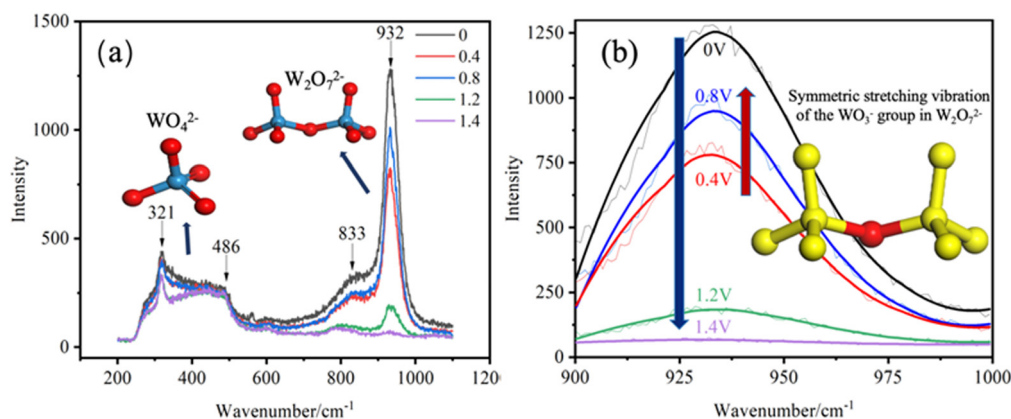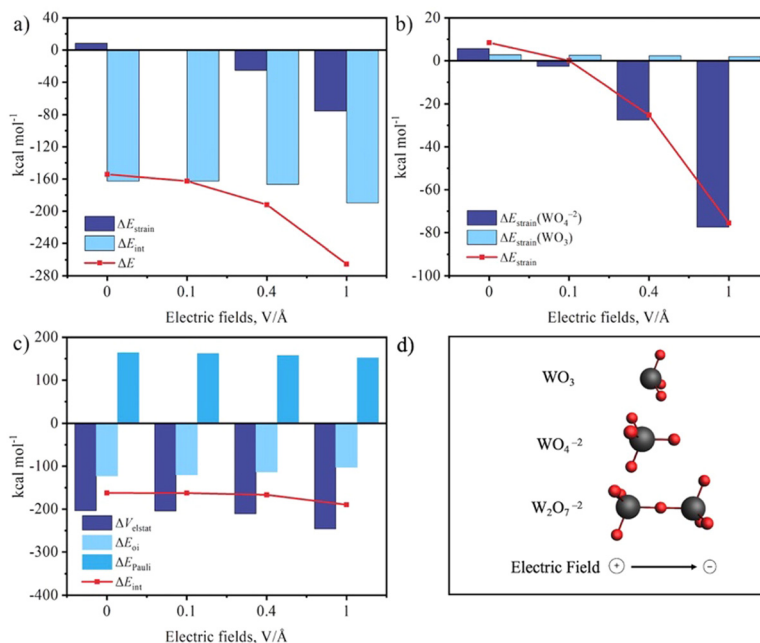

Fig. 8 (a) High-temperature *in situ* Raman data of Na$_2$WO$_4$−WO$_3$ molten salt; (b) enlarged image of Raman signal in the wavelength range of 900−1000 cm^{-1} (the yellow part represents the vibration bond).

6596 | *Phys. Chem. Chem. Phys.*, 2024, **26**, 6590−6599

This journal is © the Owner Societies 2024

Fig. 9 Activation strain analysis of $O_4W^{2-}-WO_3$ bond in $W_2O_7^{2-}$ without the electric fields ($F = 0$) and under the electric fields ($F = 0.1, 0.4, 1.0$ V Å^{-1}). The plots of (a) ΔE, ΔE_{int} and ΔE_{strain}; (b) the plots of ΔE_{strain}, $\Delta E_{strain}["WO_4^{2-}"]$ and $\Delta E_{strain}["WO_3"]$; (c) the plots of ΔE_{int}, ΔE_{oi}, ΔV_{elstat} and ΔE_{Pauli} ΔE_{strain}; (d) geometry of WO_3, O_4W^{2-} and $W_2O_7^{2-}$ under the electric fields ($F = 0.1$) computed at ZORA-PBE/TZ2P.

energy terms are shown in Fig. 9. As the electric field becomes stronger, the bonding energy ΔE values increase significantly, from -154.1 to -162.6, -191.9 and -265.3 kcal mol^{-1} which agree with our conclusion from experiments and AIMD simulation that the electric field can promote the formation of $W_2O_7^{2-}$. The bonding energy can be further decomposed into the sum of ΔE_{int} and ΔE_{strain}, both of which contribute to the stabilization of the W–O bond. The deformation of the reactant (ΔE_{strain}), especially the geometric change of WO_4^{2-}, which goes from a tetrahedral structure to a triangular pyramid, as shown in Fig. 9d, causes a larger dipole moment and subsequently leads to a larger strain energy change. In addition, as expected, the electrostatic attraction (V_{elstat}) corresponding to the classical Coulomb interaction increases as the electric field becomes strong which is in line with studies on the effect of the oriented external electric fields on Diels–Alder (DA)

reactions.[46,47] The electric field can cause the separation of the charge density,[43] as illustrated by Fig. 9, which strengthens the electrostatic attraction between two fragments.

As shown in Fig. 10, the electron density difference diagrams of $W_2O_7^{2-}$, WO_4^{2-}, and WO_3 with and without electric field were calculated (isosurface: 0.001). After optimizing the geometry of the system, CP2K was used to calculate the electron density of $W_2O_7^{2-}$, WO_4^{2-} and WO_3 under 0 V and 1.2 V electric fields, respectively. The difference processing of electron density and electron transfer number are calculated based on Multiwfn.[39] The green part in the figure presents an increase in charge, and the blue part indicates the decrease, relatively. The increasing direction of the abscissa is the direction of the electric field, and the ordinate is the electron transfer number. The electrons in the WO_4^{2-} and WO_3 systems migrate in the opposite direction of the electric field. Taking the green part as
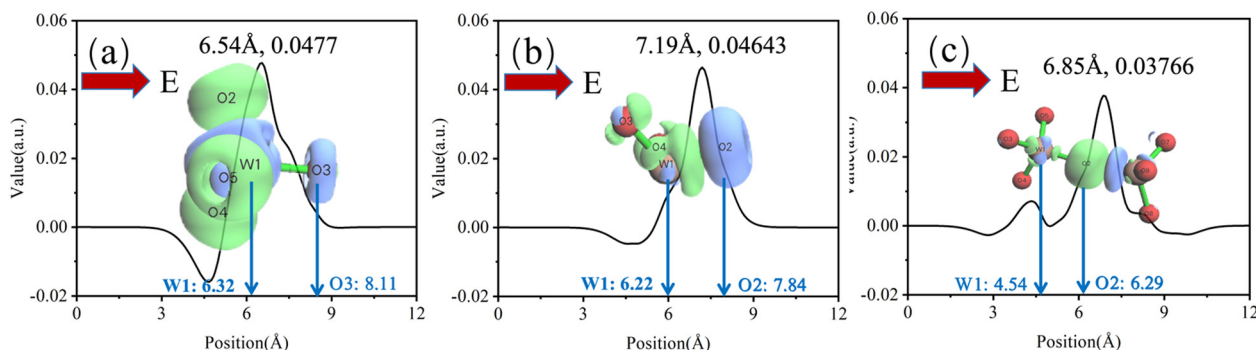
Fig. 10 Density difference plots of WO_4^{2-} (a), WO_3 (b) and $W_2O_7^{2-}$ (c) (the green part presents an increase in charge, and the blue part indicates the decrease).

This journal is © the Owner Societies 2024

Phys. Chem. Chem. Phys., 2024, **26**, 6590–6599 | **6597**

the charge center, the O_3 of WO_4^{2-} in Fig. 10a is readily attracted to the charge center of W1 of WO_3 in Fig. 10b to promote the formation of $Na_2W_2O_7$. $Na_2W_2O_7$ with a symmetrical structure has the smallest number of electron transfers in an electric field. This is somewhat related to the conclusion of the response of a centrally symmetric structure to an electric field proposed by Nardo *et al.*[48] This structure has the smallest degree of polarization.

To sum up, in the electrochemical impedance test and electrochemical deposition experiment, we proved that the addition of WO_3 allowed the tungsten in the Na_2WO_4 molten salt to be deposited at a lower voltage, which is mainly because the $Na_2W_2O_7$ generated by the reaction of Na_2WO_4 and WO_3 has a lower decomposition voltage. We used DPMD to train the data of Na_2WO_4's AIMD with CP2K to obtain deep potential. With the molecular dynamics simulations and high-temperature *in situ* Raman tests, we proved that the polarization effect of the ionic groups in the molten salt caused more $Na_2W_2O_7$ to be generated. The simulation of the electron density difference plot also proves the promoting effect of the electric field on the generation of $Na_2W_2O_7$.

Conclusions

This work employs both experiments and machine learning-based molecular dynamics simulations to analyse the effect of electric field on the distribution of tungsten in Na_2WO_4–WO_3 molten salt. Extended deep potential-based molecular dynamics simulation under different temperature and electric field conditions, using only systems similar to the training data, was demonstrated accuracy in high-temperature *in situ* Raman tests on molten salt. First, the experiment shows that after adding WO_3, the deposition voltage of tungsten in the Na_2WO_4–WO_3 system is lower than that of pure Na_2WO_4 molten salt. Next, Combining the results of molecular dynamics simulations based on deep potential and high-temperature in-site Raman testing, we found that Na_2WO_4 and WO_3 react to generate $Na_2W_2O_7$, which has a lower decomposition voltage than Na_2WO_4, allowing the deposition of tungsten to be performed under lower voltage conditions. Furthermore, the polarization effect exerted by the electric field on the ionic groups in the system increases the tendency of $Na_2W_2O_7$ to be generated in the molten salt, which is also conducive to the deposition of tungsten in the system. We calculated the W–O bond length of 1.782 Å in the simulation results, which is the unique W–O bond length of $Na_2W_2O_7$. When the voltage increased from 0 V to 1.2 V, the W–O bond content in the system increased from 6.7% to 21.5%. The calculation of electron density and bond strength provides a more specific explanation for the generation of more $Na_2W_2O_7$ in the system with the electric field. This work demonstrates the feasibility of molecular dynamics based on deep potential in tungsten molten salts and analyzes the effect of electric field on the microstructure of molten salts. This provides an important theoretical basis for understanding the behavior of ions in molten salt electrodeposition.

Author contributions

Yuliang Guo: conceptualization, validation, visualization, writing – original draft. Xiaobo Sun: investigation, writing – review & editing. Handong Jiao: Raman testing assistance, Wenxuan Qin: electrochemical experiments assistance. Xiaoli Xi: methodology, supervision, writing – review & editing. Zuoren Nie: supervision, project administration, resources.

Conflicts of interest

There are no conflicts to declare.

Acknowledgements

Notes and references

1 W. Qin, X. Xi, L. Zhang, M. Wang and Z. Nie, *Surf. Coat. Technol.*, 2022, **440**, 128497.

2 Z. Chen, M. Qin, J. Yang, L. Zhang, B. Jia and X. Qu, *J. Mater. Sci. Technol.*, 2020, **58**, 24–33.

3 M. Feng, X. Xi, L. Zhang and Z. Nie, *J. Phys. Chem. C*, 2022, **126**, 15528–15537.

4 W. Qin, X. Xi, Q. Zhang, L. Zhang, L. Ma and Z. Nie, *Int. J. Electrochem. Sci.*, 2019, **14**, 10420–10430.

5 N.-b Sun, Y.-c Zhang, F. Jiang, S.-t Lang and M. Xia, *Fusion Eng. Des.*, 2014, **89**, 2529–2533.

6 N. Sun, Y. Zhang, S. Lang, L. Wang and L. Wang, *J. Fusion Energy*, 2015, **34**, 1417–1422.

7 F. Jiang, Y. Zhang, N. Sun and J. Leng, *Appl. Surf. Sci.*, 2015, **327**, 432–436.

8 H. Lu, J. Qin, C. Di, Y. Yang and R. Huo, *Mater. Trans.*, 2018, **59**, 1943–1948.

9 K. Nitta, T. Nohira, R. Hagiwara, M. Majima and S. Inazawa, *Electrochim. Acta*, 2010, **55**, 1278–1281.

10 T. Nohira, T. Ide, X. Meng, Y. Norikawa and K. Yasuda, *J. Electrochem. Soc.*, 2021, **168**, 046505.

11 Y. Tian, L. Ma, X. Xi and Z. Nie, *J. Electroanal. Chem.*, 2022, **921**, 116700.

12 Y. Qi, Y. Tang, B. Wang, M. Zhang, X. Ren, Y. Li and Y. Ma, *Int. J. Refract. Met. Hard Mater.*, 2019, **81**, 183–188.

13 H. Nakajima, T. Nohira and R. Hagiwara, *Electrochem. Solid-State Lett.*, 2005, **8**, C91–C94.

14 D. Jihong, L. Zhengxiang, L. Gaojian, Z. Hui and H. Chunliang, *Surf. Coat. Technol.*, 2005, **198**, 169–172.

15 A. Kobayashi, S. Sharafat and N. M. Ghoniem, *Surf. Coat. Technol.*, 2006, **200**, 4630–4635.

6598 | *Phys. Chem. Chem. Phys.*, 2024, **26**, 6590–6599

This journal is © the Owner Societies 2024

16 V. A. Pavlovskii, *Prot. Met.*, 2006, **42**, 170–173.

17 Z. Lian, X. Fang, W. Han, J. Yu, Z. Wang, Y. Zhang and K. Zhu, *Fusion Eng. Des.*, 2016, **112**, 136–142.

18 F. Jiang, *Appl. Surf. Sci.*, 2016, **363**, 389–394.

19 F. Jiang and Y. Zhang, *J. Fusion Energy*, 2018, **37**, 255–260.

20 Y. H. Liu, Y. C. Zhang, Q. Z. Liu, X. L. Li and F. Jiang, *Fusion Eng. Des.*, 2012, **87**, 1861–1865.

21 F. Jiang, S. Shao and H. Wu, *Fusion Eng. Des.*, 2016, **106**, 71–76.

22 M. Feng, X. Xi, L. Zhang and Z. Nie, *J. Mol. Liq.*, 2022, **355**, 118944.

23 M. Feng, X. L. Xi, L. W. Zhang and Z. R. Nie, *Phys. Chem. Chem. Phys.*, 2022, **24**, 20130–20137.

24 G. Cassone, J. Sponer and F. Saija, *Top. Catal.*, 2021, **65**, 40–58.

25 D. Lu, H. Wang, M. Chen, L. Lin, R. Car, W. E, W. Jia and L. Zhang, *Comput. Phys. Commun.*, 2021, **259**, 107624.

26 Y. Shi, S. T. Lam and T. L. Beck, *Chem. Sci.*, 2022, **13**, 8265–8273.

27 L. Zhang, J. Han, H. Wang, R. Car and W. E, *Phys. Rev. Lett.*, 2018, **120**, 143001.

28 W. Liang, G. Lu and J. Yu, *ACS Appl. Mater. Interfaces*, 2021, **13**, 4034–4042.

29 M. Bu, T. Feng and G. Lu, *J. Mol. Liq.*, 2023, **375**, 120689.

30 M. Bu, W. Liang, G. Lu and J. Yu, *Sol. Energy Mater. Sol. Cells*, 2021, **232**, 111346.

31 J. Zhao, Y. Wang and G. Lu, *J. Electrochem. Soc.*, 2022, **169**, 056517.

32 T. Xu, X. Li, Y. Wang and Z. Tang, *ACS Appl. Mater. Interfaces*, 2023, **15**, 14184–14195.

33 T. D. Kuhne, M. Iannuzzi, M. Del Ben, V. V. Rybkin, P. Seewald, F. Stein, T. Laino, R. Z. Khaliullin, O. Schutt, F. Schiffmann, D. Golze, J. Wilhelm, S. Chulkov, M. H. Bani-Hashemian, V. Weber, U. Borstnik, M. Taillefumier, A. S. Jakobovits, A. Lazzaro, H. Pabst, T. Muller, R. Schade, M. Guidon, S. Andermatt, N. Holmberg, G. K. Schenter, A. Hehn, A. Bussy, F. Belleflamme, G. Tabacchi, A. Gloss, M. Lass, I. Bethune, C. J. Mundy, C. Plessl, M. Watkins, J. VandeVondele, M. Krack and J. Hutter, *J. Chem. Phys.*, 2020, **152**, 194103.

34 A. P. Thompson, H. M. Aktulga, R. Berger, D. S. Bolintineanu, W. M. Brown, P. S. Crozier, P. J. in 't Veld, A. Kohlmeyer, S. G. Moore, T. D. Nguyen, R. Shan, M. J. Stevens, J. Tranchida, C. Trott and S. J. Plimpton, *Comput. Phys. Commun.*, 2022, **271**, 108171.

35 H. Jiao, J. An, Y. Jia, Q. Liu, Z. Wang, Y. Gao, M. Wang, D. Fang, H. Zhu and S. Jiao, *Proc. Natl. Acad. Sci. U. S. A.*, 2023, **120**, e2301780120.

36 H. Wang, L. Zhang, J. Han and W. E, *Comput. Phys. Commun.*, 2018, **228**, 178–184.

37 D. Lu, W. Jiang, Y. Chen, L. Zhang, W. Jia, H. Wang and M. Chen, *J. Chem. Theory Comput.*, 2022, **18**, 5559–5567.

38 J. Hutter, M. Iannuzzi, F. Schiffmann and J. VandeVondele, *Wiley Interdiscip. Rev.: Comput. Mol. Sci.*, 2014, **4**, 15–25.

39 T. Lu and F. Chen, *J. Comput. Chem.*, 2012, **33**, 580–592.

40 K. He, X. Zhang, S. Ren and J. Sun, presented in part at the 2016 IEEE Conference on Computer Vision and Pattern Recognition (CVPR), 2016.

41 S. ADF, Theoretical Chemistry, Vrije Universiteit, (**https://www.scm.com**).

42 K. N. H. F. M. Bickelhaupt, *Angew. Chem., Int. Ed.*, 2017, **56**, 10070–10086.

43 T. M. S. X. Sun, J. Poater, T. A. Hamlin and F. M. Bickelhaupt, *J. Comput. Chem.*, 2019, **40**, 2227–2233.

44 J. Wang, J. L. You, A. A. Sobol, L. M. Lu, M. Wang, J. Wu, X. M. Lv and S. M. Wan, *J. Raman Spectrosc.*, 2017, **48**, 298–304.

45 J. Wang, J. You, M. Wang, L. Lu, S. Wan and A. A. Sobol, *Spectrochim. Acta, Part A*, 2017, **185**, 188–196.

46 D. M. S. Shaik and R. Ramanan, *Nat. Chem.*, 2016, **8**, 1091–1098.

47 P. V. S. Yu, T. A. Hamlin and F. M. Bickelhaupt, *Chem. – Eur. J.*, 2021, **27**, 5683–5693.

48 V. Mollica Nardo, G. Cassone, R. C. Ponterio, F. Saija, J. Sponer, M. Tommasini and S. Trusso, *J. Phys. Chem. A*, 2020, **124**, 10856–10869.

This journal is © the Owner Societies 2024

Phys. Chem. Chem. Phys., 2024, **26**, 6590–6599 | **6599**